remote sensing

MDPI

Article

On-Orbit Vicarious Radiometric Calibration and Validation of ZY1-02E Thermal Infrared Sensor

Hongzhao Tang [1], Junfeng Xie [1,*], Xianhui Dou [1], Honggeng Zhang [1,2] and Wei Chen [2]

[1] Land Satellite Remote Sensing Application Center, Ministry of Natural Resources, Beijing 100094, China
[2] College of Geoscience and Surveying Engineering, China University of Mining and Technology (Beijing), Beijing 100083, China
* Correspondence: xiejf@lasac.cn; Tel.: +86-10-6841-2293

Abstract: The ZY1-02E satellite carrying a thermal infrared sensor was successfully launched from the Taiyuan Satellite Launch Center on 26 December 2021. The quantitative characteristics of this thermal infrared camera, for use in supporting applications, were acquired as part of an absolute radiometric calibration campaign performed at the Ulansuhai Nur and Baotou calibration site (Inner Mongolia, July 2022). In this paper, we propose a novel on-orbit absolute radiometric calibration technique, based on multiple ground observations, that considers the radiometric characteristics of the ZY1-02E thermal infrared sensor. A variety of natural surface objects were selected as references, including bodies of water, bare soil, a desert in Kubuqi, and sand and vegetation at the Baotou calibration site. During satellite overpass, the 102F Fourier transform thermal infrared spectrometer and the SI-111 infrared temperature sensor were used to measure temperature and ground-leaving radiance for these surface profiles. Atmospheric water vapor, aerosol optical depth, and ozone concentration were simultaneously obtained from the CIMEL CE318 Sun photometer and the MICROTOP II ozonometer. Atmospheric profile information was acquired from radiosonde instruments carried by sounding balloons. Synchronous measurements of atmospheric parameters and ECMWF ERA5 reanalysis data were then combined and input to an atmospheric radiative transfer model (MODTRAN6.0) used to calculate apparent radiance. Calibration coefficients were determined from the measured apparent radiance and satellite-observed digital number (DN), for use in calculating the on-orbit observed radiance of typical surface objects. These values were then compared with the apparent radiance of each object, using radiative transfer calculations to evaluate the accuracy of on-orbit absolute radiometric calibration. The results show that the accuracy of this absolute radiometric calibration is better than 0.6 K. This approach allows the thermal infrared channel to be unrestricted by the limitations of spectrum matching between a satellite and field measurements, with strong applicability to various types of calibration sites.

Keywords: ZY1-02E; thermal infrared sensor; radiometric calibration; Ulansuhai Nur

Citation: Tang, H.; Xie, J.; Dou, X.; Zhang, H.; Chen, W. On-Orbit Vicarious Radiometric Calibration and Validation of ZY1-02E Thermal Infrared Sensor. *Remote Sens.* **2023**, *15*, 994. https://doi.org/10.3390/rs15040994

Academic Editor: Pablo Rodríguez-González

Received: 30 December 2022
Revised: 28 January 2023
Accepted: 8 February 2023
Published: 10 February 2023

1. Introduction

Thermal infrared remote sensing involves analyzing critical parameters, such as surface and atmospheric temperature information, specific surface emissivity, and atmospheric composition content by measuring infrared radiation signals from the Earth's surface and atmosphere. Thermal infrared remote sensing data exhibit the characteristics of wide coverage and long time spans for continuous monitoring. As such, these measurements are frequently applied in the fields of global climate change, surface energy balance, surface temperature retrieval, atmospheric detection, hydrological monitoring, disaster warning, environmental pollution monitoring, and geothermal detection [1–3]. During the development of thermal infrared remote sensing in the aerospace field for more than 60 years, multiple satellites were launched with onboard infrared sensors. This included TIROS-1, METEOSAT, NOAA, LANDSAT, TERRA, HJ, and FY, providing the means to obtain large-scale land, water, and atmospheric information [4–6].

The absolute radiometric calibration of thermal infrared cameras is a key technology for quantitative applications in remote sensing. In the Global Climate Change Satellite Calibration Workshop 2002, a new goal was proposed for the accuracy and stability of satellite-based thermal radiation observations. The accuracy of satellite thermal radiation observation should be 0.1 K and the stability should be less than 0.04 K per decade [7]. To achieve this goal, it will be necessary to calibrate observation data from satellite sensors with a uniform benchmark, accurately monitor sensor performance changes while in orbit, ensure the consistency of observational data, and measure the stability of mass data [8]. The observational accuracy of thermal infrared sensors can be assessed using various on-orbit calibration techniques [9]. For example, after improving the USGS/EROS data processing system, Barsi conducted on-orbit radiometric calibration and verification for a Landsat 8 TIRS thermal infrared channel. The final calibration result was improved to better than 0.5 K [10]. Okuyama recalibrated the visible and near-infrared channels of VISSR on the GMS-5 satellite by combining reanalysis, ground observation, and MODIS data, identifying calibration coefficients with greater temporal stability [11]. Schott calibrated observed values based on the MODTRAN model by combining NCEP reanalysis and historical water leaving-radiation data, with an observed uncertainty reaching 0.6 K after calibration [12]. Zhang performed an absolute calibration of the CBERS-02IRMSS thermal infrared channel using the calibration field from Qinghai Lake, achieving a result similar to blackbody satellite calibration by combining this approach with MODIS cross-calibration [13]. Rong and Hu compared field calibration results from the FY-2B and FY-2C thermal infrared channels with laboratory calibration data, achieving the expected results within 2 K [14]. Han used observation and Landsat 5 TM data to verify calibration coefficients for the HJ-1B site, improving the overall accuracy by 1 K [15]. Liu obtained absolute calibration coefficients for the HJ-1BIRS thermal infrared channel using field-measured data and onboard blackbody calibration results, verified in the Dari Lake area of Inner Mongolia [16].

ZY1-02E successfully entered a scheduled orbit at Taiyuan Satellite Launch Center on a Long March 4C carrier rocket at 11:11 AM on December 26, 2021. It is China's second independent civil natural resource hyperspectral operation satellite. In addition to a 9-band multispectral camera (VNIC) and a 166-band hyperspectral camera (AHSI) onboard ZY1-02D, ZY1-02E carries a new thermal infrared sensor (IRS) that can effectively acquire images with a spatial resolution of better than 16 m and a width of 115 km. This provides important data support for China's natural resources survey, geological monitoring, and other environmental services. For instance, rapid and accurate acquisition of surface temperature has become one of the keys to improving remote sensing capabilities for natural resource surveys. The advantages of the ZY1-02E thermal infrared camera can be fully utilized by evaluating the on-orbit stability of the satellite and conducting a radiation accuracy evaluation.

Owing to the extreme conditions of space and associated component aging, radiation characteristics for the infrared emission spectrum cannot be adequately described by pre-launch laboratory calibration tests. Therefore, it is necessary to regularly conduct on-orbit absolute radiation calibrations for the satellite load. In July 2022, a ground-synchronous observation test was conducted for ZY1-02E at the national high-resolution integrated calibration field in Ulansuhai Lake and at Baotou in Bayannur City. The thermal infrared camera was calibrated using absolute radiation from the orbit site and further accuracy verification analysis. Domestic researchers used a technique based on radiometry for the thermal infrared channels on FY and HJ1-B series satellites. In this process, a multichannel thermal infrared radiometer (CE312) was used to obtain synchronous ground radiance. Satellite ground spectrum matching was then applied to measure the radiance of incident optical radiance from the onboard thermal infrared channels. However, because the band design for the ZY1-02E thermal infrared camera differs from the channel spectrum of CE312, it can be difficult to obtain radiance information by direct observation and spectral matching, as conventional radiance-based methods are not applicable to this camera. As such, this paper proposes an on-orbit absolute radiometric calibration for ZY1-02E, based on a variety of natural objects. With this approach, the thermal infrared channel is not subject to the requirements of satellite ground spectrum matching and is highly robust for adaptation to various types of ground radiation calibration sites.

2. Materials and Methods

2.1. ZY1-02E Satellite and Thermal Infrared Camera

ZY1-02E is China's second independent civil natural resource hyperspectral service satellite, equipped with multiple cameras covering the typical bands of visible, near-infrared, short-wave infrared, and thermal infrared. ZY1-02E also has an additional thermal infrared camera to observe ground temperature. The satellite load exhibits prominent quantitative characteristics and is positioned for medium resolution large-scale observations and remote sensing tasks. Technical parameters for the satellite are provided in Table 1 and the spectral response function for the thermal infrared camera is shown in Figure 1.

Table 1. ZY1-02E and thermal IRS parameters.

	Classification of Track	**Sun Synchronously Returns to Orbit**
Orbit	Orbital Altitude Orbital Inclination Local Time of Descending Node Side Swing Ability Return Cycle	778.099 km 98.5° 10:30 a.m. ±32° 55 days
Thermal Infrared Camera **Sensor1** **Sensor2**	Spectral Range Subsatellite Resolution Scanning Width Digitizing Bit	7.7 µm–10.5 µm 16 m 115 km 12 bit

Figure 1 shows the spectral response function of the thermal infrared camera.

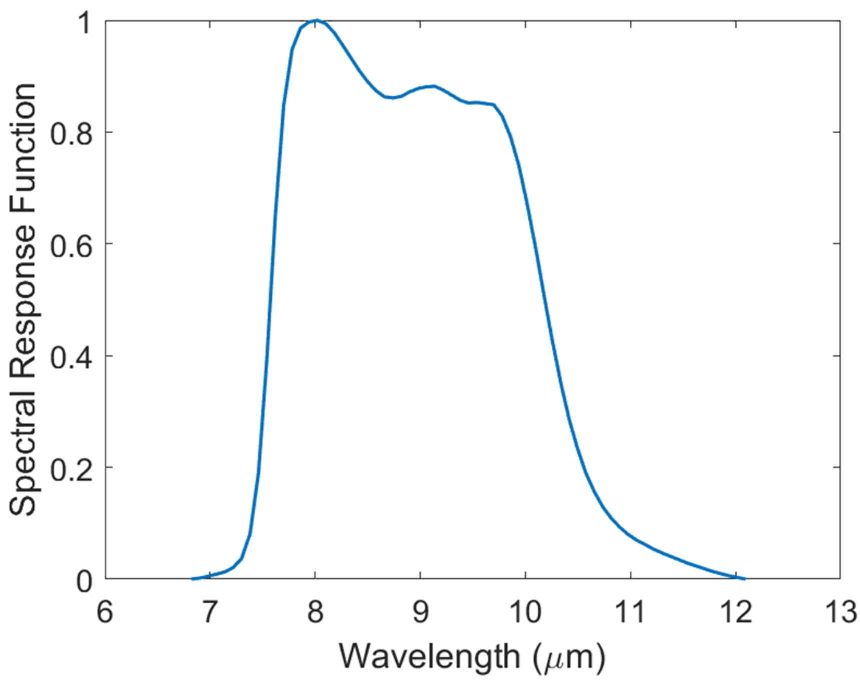

Figure 1. The spectral response function for the thermal infrared camera (sensor1 and sensor2).

2.2. On-Orbit Vicarious Absolute Radiometric Calibration Method

In this study, we propose an on-orbit absolute radiometric calibration and verification technique for thermal infrared cameras, based on a variety of homogeneous natural objects including bodies of water, bare soil, a desert in Kubuqi, and sand and vegetation at the Baotou calibration site. During satellite overpass, a 102F Fourier transform thermal infrared spectrometer and an SI-111 infrared temperature sensor were used to measure the temperature and ground-leaving radiance of these surface objects. A CE318 automatic solar photometer and an ozonometer were used to measure atmospheric water vapor, aerosols, and ozone at the time of satellite transit. An atmospheric radiation transport model (MODTRAN) was then combined with a reanalysis database provided by ECMWF ERA5 and atmospheric profile information collected by a sounding balloon, to calculate the at-sensor radiance of the satellite load. Calibration coefficients were determined from the measured apparent radiance and the satellite-observed digital number (DN). Using radiative transfer calculations to evaluate the accuracy of the on-orbit absolute radiometric calibration, the on-orbit observed radiance of typical surface objects was then calculated and compared with the apparent radiance, as demonstrated in Figure 2.

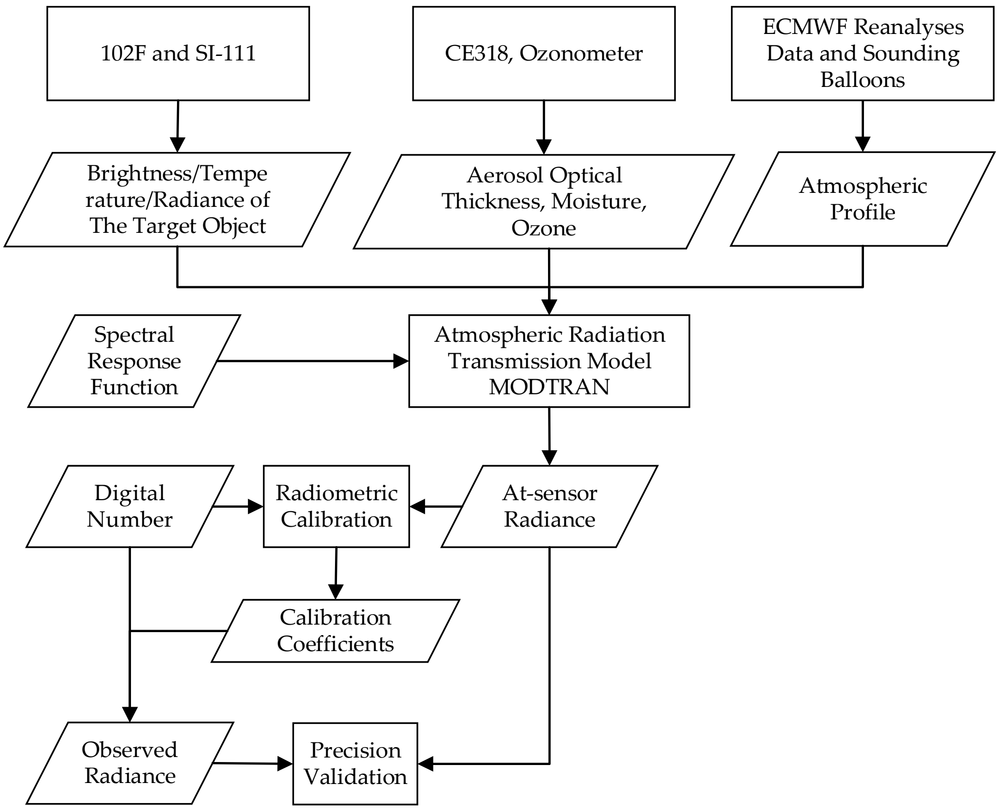

Figure 2. ZY1-02E on-orbit absolute radiation calibration and accuracy verification.

2.3. Test Area

2.3.1. Ulansuhai Nur

Ulansuhai Nur is in the territory of Wulateqian Banner in Bayannur City, Inner Mongolia, and the triangle edge of Hohhot, Baotou, and Ordos, as demonstrated in Figures 3 and 4. The site is 13 km from the government of Wulashan town and features a river-track lake formed by diversion of the Yellow River. With a total area of 300 square kilometers, it is one of the eight major freshwater lakes in China and is known as "Pearl of the Seaside". The large area, high specific heat capacity, shallow depths (average depth of ~1.5 m and maximum depth of ~4 m), and stable temperatures exhibited by the lake make it a preferred calibration source for thermal infrared remote sensing. Several regions consisting of bare soil can also be found around Ulansuhai Nur, with flat and uniform surfaces for use as calibration sources.

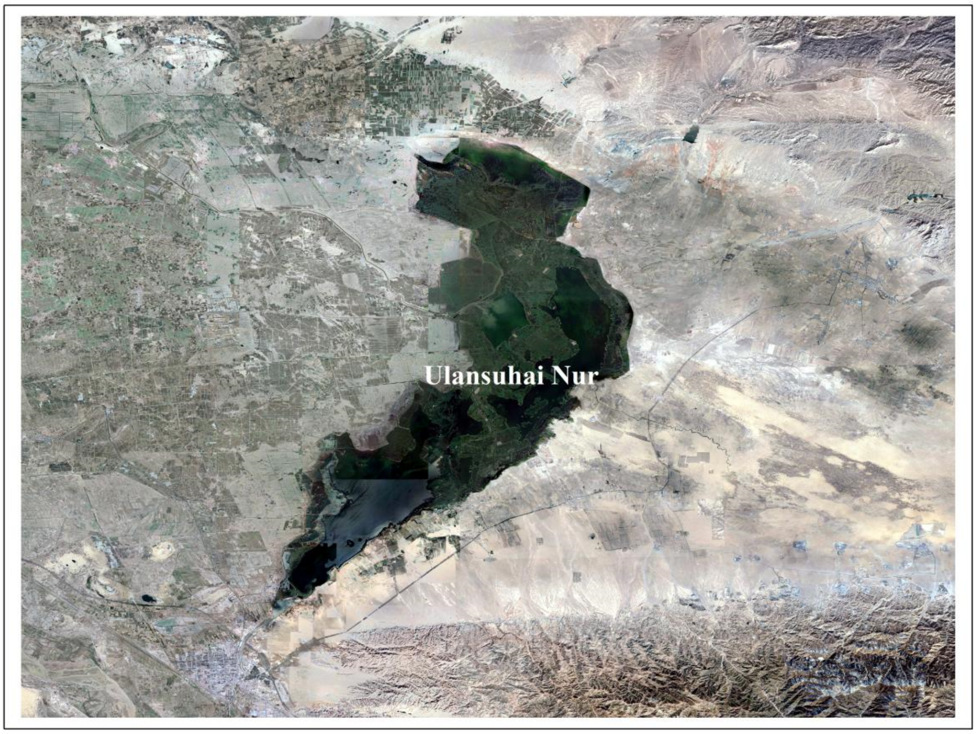

Figure 3. An aerial image of Ulansuhai Nur.

Figure 4. Images of water and bare soil in Ulansuhai Nur.

2.3.2. Baotou Site

The Baotou site is a comprehensive calibration facility managed by the Institute of Optoelectronics of the Chinese Academy of Sciences, under continuous support from the key project of "Unmanned Remote Sensing Comprehensive Verification System" of "the 12th Five-Year Plan" of the Ministry of Science and Technology of China (MSTC). The calibration field has been approved by MSTC and has been officially listed as a "National High-Resolution Remote Sensing Integrated Calibration Site" by the National Remote Sensing Center of the MSTC. Baotou was also included in the first batch of demonstration sites for the CEOS Global Autonomous Radiation Calibration Network (RadCalNet). The location includes flat terrain with an elevation range 1037–1289 m and an average elevation of 1270 m. Located 20 km east of Wuliangsu Lake, Baotou includes a large region of uniform sand covering an area of 300×300 m^2 and a region of uniform vegetation covering an area of 900×450 m^2.

2.3.3. Kubuqi Desert

Kubuqi Desert, as demonstrated in Figure 5, is the seventh largest desert in China and located ~50 km south of Wuliangsu Lake. The region features flat sand and is 400 km long and 50 km wide, with a total area of ~13,900 square kilometers.

Figure 5. An image of Kubuqi Desert.

2.4. The Vicarious Radiometric Calibration Campaign

2.4.1. Acquisition of Surface Parameters

Surface parameters were primarily obtained using a 102F portable Fourier transform thermal infrared spectrometer and an SI-111 infrared temperature sensor. The spectrometer is mainly composed of a miniature Michelson interferometer, a sampling lens, a blackbody reference, an optical component, electronic equipment, and a composite detector used to measure off-ground radiance and emissivity spectral information from ground object targets at the time of satellite overpass. Figure 6 shows the 102F portable Fourier transform thermal infrared spectrometer in different locations.

Figure 6. The emissivity of typical ground objects measured by 102F.

The temperature sensor, consisting of a thermopile and a thermistor, was used to quantify target brightness by measuring a millivoltage resistance signal for input to the Stefan–Boltzmann equation. Figure 7 shows the SI-111 infrared temperature sensor in different locations.

Figure 7. Experimental deployment of the SI-111 infrared temperature sensor.

2.4.2. Acquisition of Atmospheric Parameters

Atmospheric parameters such as temperature, humidity, and pressure were acquired at the time of satellite transit using data from a sounding balloon. The ECMWF reanalysis database also provided global effective temperature, humidity, and pressure profiles with a time interval of 1 h, a maximum spatial resolution of 0.1°, and 37 layers from 1000 to 1 hPa. A CE318 automatic solar photometer was used to measure atmospheric aerosol content and water vapor during transit, while the MICROTOPSII handheld ozonometer was used to calculate the total amount of ozone by measuring direct solar ultraviolet radiation at five discontinuous wavelengths in the ultraviolet range of UVB.

3. Results

3.1. Radiative Transfer Simulations for At-Sensor Radiance

3.1.1. Thermal Infrared Radiation Transfer Equation

Under the conditions of a clear sky, atmospheric uniformity, and local thermal equilibrium, the energy received can be expressed as:

$$L(T, \theta_v, \lambda) = L_G(T_G, \theta_v, \lambda)\tau_i(\theta_v, \lambda) + L_{atm\uparrow}(\theta_v, \lambda) \quad (1)$$

$$L_G(T_G, \theta_v, \lambda) = \varepsilon_i(\theta_v, \lambda)B(T_S, \lambda) + (1 - \varepsilon_i(\theta_v, \lambda))L_{atm\downarrow}(\theta_v, \lambda) \quad (2)$$

where $L(T, \theta_v, \lambda)$ is radiance measured by the satellite sensor; $L_G(T_G, \theta_v, \lambda)$ is the total spectral radiance of the surface (the off-ground radiance); $\tau_i(\theta_v, \lambda)$ is the atmospheric transmittance from the surface to the sensor; T and T_G are, respectively, the on-board brightness and surface brightness temperatures; θ_v is the observed zenith angle; λ is the wavelength; ε_i is the emissivity of the ground object; B is the Planck function; $L_{atm\downarrow}(\theta_v, \lambda)$ is the downward radiation of the atmosphere; and $L_{atm\uparrow}(\theta_v, \lambda)$ is the upward radiation of the atmosphere.

3.1.2. Acquisition of Off-Ground Radiance $L_G(T_G, \theta_v, \lambda)$

Tests involving water targets used a 102F portable Fourier transform thermal infrared spectrometer to synchronously measure the off-water radiance $L_G(T_G, \theta_v, \lambda)$ during satellite transit. Atmospheric parameters such as transmittance $\tau_i(\theta_v, \lambda)$ and atmospheric upward radiation $L_{atm\uparrow}(\theta_v, \lambda)$ were then determined and at-sensor radiance was calculated through combination with a spectral response function. Tests utilizing other ground targets used an SI-111 infrared temperature sensor to measure off-ground brightness temperatures during transit. A temperature–radiance lookup table established from Planck's law was then applied to convert these data to off-ground radiance values. However, owing to the varied spectral response of SI-111 and the satellite thermal infrared channels, this conversion relationship must be established by combining the target emissivity spectrum with the spectral response function of both sensors. The 102F spectrometer was also used to measure off-ground radiance for ground targets and the surface emissivity spectrum was then reconstructed with high accuracy using OMP constraints. An over-complete sparse dictionary D_ε of emissivity spectral features was further established using OMP and the K-SVD algorithm to separate surface object temperature from emissivity data. The sparse unknown emissivity values could then be represented as:

$$B(T_{gi}) = D_\varepsilon x_t B(T_s) \quad (3)$$

where T_s denotes the number of nonzero surface temperatures. The number of unknowns in this equation is fewer than the number of known equations, allowing the formula to be solved directly for the surface temperature and emissivity spectrum.

This process involves several technical challenges, including interference from atmospheric noise and a final solution that may not be unique. As such, statistical characteristics of the emissivity spectrum were added to provide additional constraints. Specifically, the MMD-STD method was employed, which can be described as:

$$\hat{\varepsilon}_i = \varepsilon_i / \bar{\varepsilon}_i \quad (4)$$

$$MMD = \max(\hat{\varepsilon}_i) - \min(\hat{\varepsilon}_i) \quad (5)$$

$$STD = \text{std}(\hat{\varepsilon}_i) \tag{6}$$

$$\varepsilon_{\min} = u + v_1 \times MMD^{w_1} + v_2 \times STD^{w_2} \tag{7}$$

where $\hat{\varepsilon}_i$ is the unbiased estimated emissivity; ε_i is the measured emissivity and $\bar{\varepsilon}_i$ is the average value of the emissivity spectrum; MMD is the difference between the maximum and minimum values of the unbiased estimated emissivity; STD is the standard deviation of the unbiased estimated emissivity; $\varepsilon_{\min}$ is the minimum value of the emissivity spectrum; and u, v_1, v_2, w_1 and w_2 are empirical coefficients to be fitted.

These MMD-STD constraints on the minimum emissivity, coupled with a sparse dictionary using prior knowledge to reduce the dimension of unknowns and eliminate noncharacteristic noise, facilitated the retrieval of thermal infrared surface temperature and emissivity data given a limited number of solution conditions. Emissivity curves for water and bare soil in Ulansuhai Nur are shown in Figure 8.

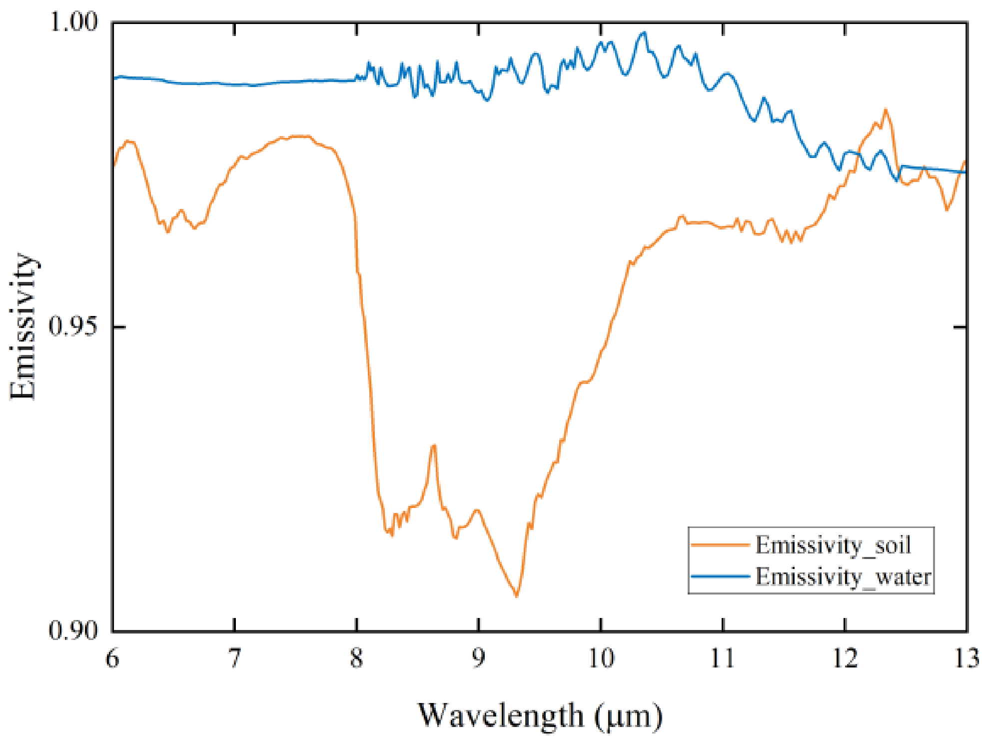

Figure 8. Emissivity curves for water and bare soil in Ulansuhai Nur.

The emissivity spectrum $\varepsilon(\lambda)$ of target ground objects could then be obtained and combined with the spectral response functions of the two sensors. The off-ground radiance conversion relationship was established as:

$$L_{G\_SI-111} = \frac{\int \varepsilon(\lambda) \cdot B(T_i, \lambda) \cdot rsf_{SI-111}(\lambda) d\lambda}{\int rsf_{SI-111}(\lambda) d\lambda} \tag{8}$$

$$L_{G\_IR} = \frac{\int \varepsilon(\lambda) \cdot B(T_i, \lambda) \cdot rsf_{IR}(\lambda) d\lambda}{\int rsf_{IR}(\lambda) d\lambda} \tag{9}$$

$$F = f(L_{G\_SI-111}, L_{G\_IR}) \tag{10}$$

and used to calculate equivalent off-ground radiance for the satellite sensor. Figure 9 shows the off-water radiance of Ulansuhai Nur.

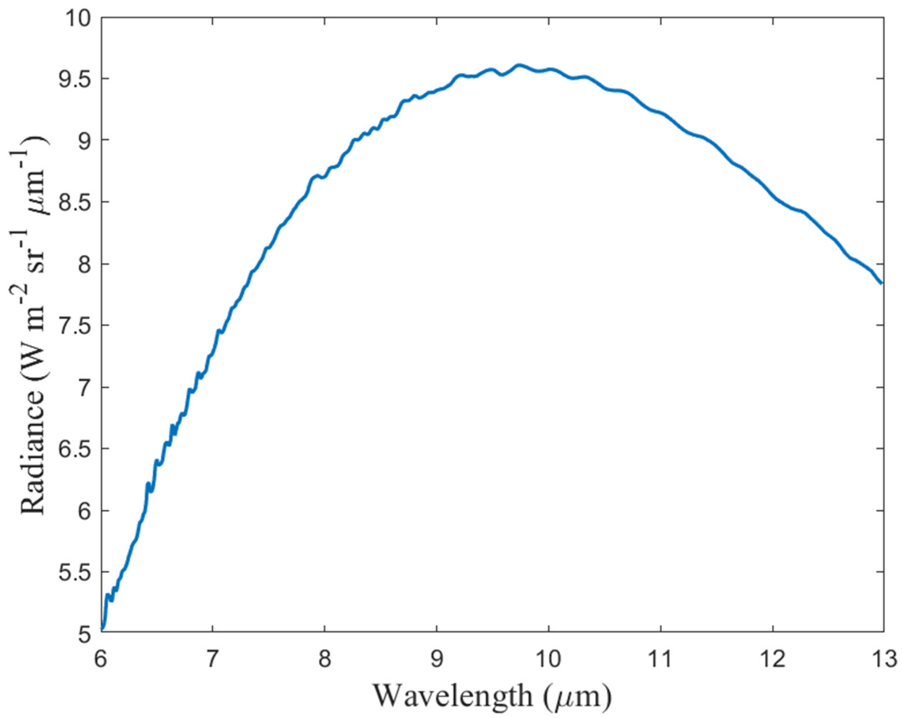

Figure 9. Off-water radiance of Ulansuhai Nur.

3.1.3. Acquisition of Atmospheric Parameters

Atmospheric profile data before and after satellite transit were directly obtained from a sounding balloon and input to the MODTRAN atmospheric radiation transmission model. Water vapor, aerosol, and ozone content were then used to calculate atmospheric transmittance and upward radiation, as it shown in Figure 10.

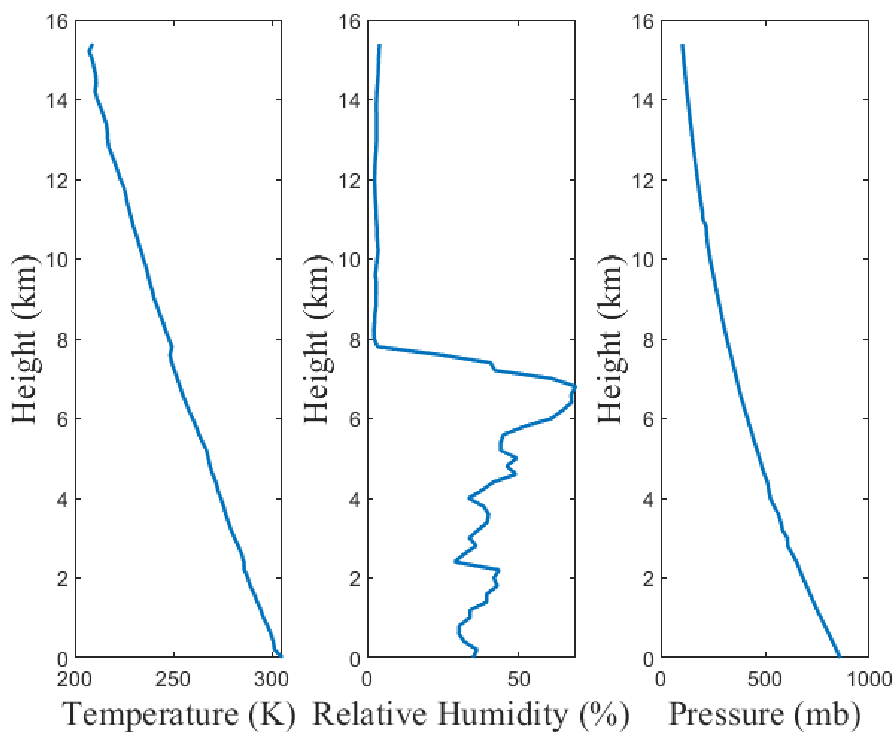

Figure 10. Atmospheric profile data from sounding balloons, including temperature, relative humidity, and atmospheric pressure.

The spatial resolution of the atmospheric profile reanalysis data provided by ECMWF was up to 0.1° × 0.1°, with temporal resolution of 1 h. The spatial resolution of the satellite infrared spectrum to be determined was relatively high and the satellite transit time was not on the order of an hour. As such, the ECMWF data needed to be interpolated in both time and space.

Temporal domain interpolation involved time data collected before and after satellite transit. A linear interpolation model was then applied to acquire reanalysis atmospheric profile data during transit as follows:

$$\phi(t) = \phi(t_a) + \frac{t - t_a}{t_{a+1} - t_a}(\phi(t_{a+1}) - \phi(t_a)) \quad (11)$$

where $\phi(t)$ refers to the atmospheric temperature, humidity, ozone content, potential, and other parameters corresponding to each layer of the atmospheric profile after interpolation. The terms t_a and t_{a+1}, respectively, denote the hour before and after the transit time.

Spatial interpolation was performed using the inverse distance weighted spatial aggregation method, adopted in this paper to aggregate atmospheric profile data (after temporal interpolation) to the pixel scale of the satellite to be determined. This inverse distance weighting algorithm is based on the principle of nearness and similarity, as each sampling point exhibits a certain influence on the interpolation points (i.e., a weight). The smaller the distance to an interpolation point, the greater the weight of the sampling point. The weight then decreases with increasing distance between sampling and interpolation points as follows:

$$z = \frac{\sum_{i=1}^{n} z_i \cdot \frac{1}{d_i}}{\sum_{i=1}^{n} \frac{1}{d_i}} \quad (12)$$

where z is the total weight, z_i is the weight of each sampling point, d_i is the Euclidean distance to each sampling point from the interpolation point, and n is the number of sampling points. Atmospheric profile information at the corresponding time and location were then obtained for input to the MODTRAN atmospheric radiative transport model. Water vapor, aerosol, and ozone content were also used to calculate atmospheric transmittance and atmospheric upward radiation, as it shown in Figure 11.

3.1.4. Brightness Acquisition by the On-Board Pupil

The on-board entry pupil radiance was calculated by combining the above thermal infrared radiation transfer equation with a spectral response function. Each step was then calculated at the channel level for other ground objects using SI-111 measurement data to obtain off-earth radiance. Since the thermal infrared channel for the target satellite was set wide, the calculated results are bound to differ significantly from the actual measurements. As such, it is necessary to correct the wide-channel response influence and establish a correction relation F-band (Equation (11)). The on-board entry pupil radiance for the thermal infrared camera could then be obtained using a wide-channel response influence correction as follows:

$$L_{spectral} = \frac{\int \left[L_G(T_G, \lambda)\tau(\lambda) + L_{atm\uparrow}(\lambda)\right] \cdot rsf_{IR}(\lambda)d\lambda}{\int rsf_{IR}(\lambda)d\lambda} \quad (13)$$

$$L_{band} = \frac{\int L_G(T_G, \lambda) \cdot rsf_{IR}(\lambda)d\lambda}{\int rsf_{IR}(\lambda)d\lambda} \cdot \frac{\int \tau(\lambda) \cdot rsf_{IR}(\lambda)d\lambda}{\int rsf_{IR}(\lambda)d\lambda} + \frac{\int L_{atm\uparrow}(\lambda) \cdot rsf_{IR}(\lambda)d\lambda}{\int rsf_{IR}(\lambda)d\lambda} \quad (14)$$

$$F_{band} = f\left(L_{spectral}, L_{band}\right) \quad (15)$$

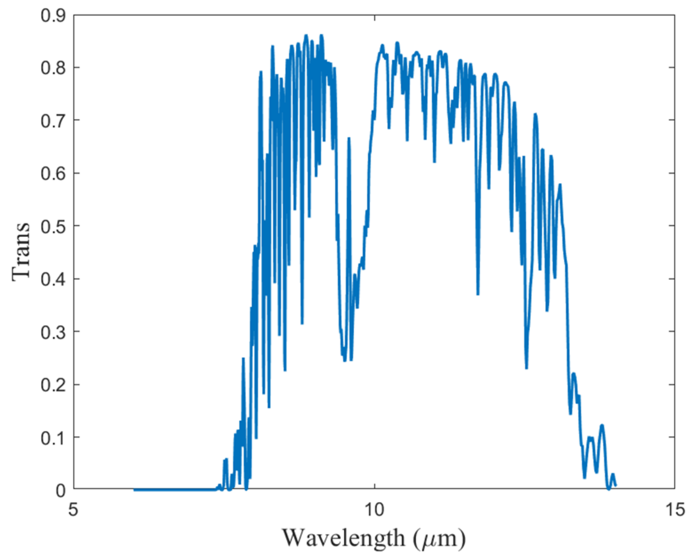

(**a**)

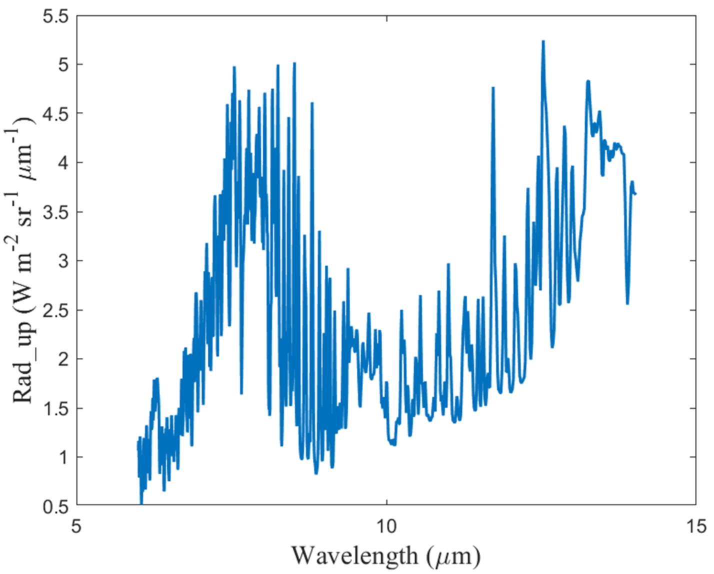

(**b**)

Figure 11. Atmospheric transmittance and upward radiation obtained by ECMWF for sensor1 and sensor2: (**a**) atmospheric transmittance; (**b**) upward radiation.

3.2. Radiometric Calibration Results

Ground measurement data and atmospheric parameters for typical high- and low-temperature ground objects, synchronously acquired above, were calculated using the MODTRAN radiative transmission model to obtain the radiance of the on-board pupil. The gain and bias (calibration coefficients) were determined using a calibration formula (Equations (13)–(15)), combined with a digital quantization value (DN) for each image observed by the satellite load. The resulting radiance was then:

$$Radiance = Gain \cdot DN + Bias \tag{16}$$

It is worth noting the ZY1-02E thermal infrared camera system (IRS) involves two sets of loads with the same design parameters, Sensor1 (main component) and Sensor2 (backup), which image simultaneously. Therefore, in addition to radiometric calibration of the IRS principal camera (Sensor1), calibration and accuracy verification were also conducted for the backup camera (Sensor2).

Thermal infrared images from ZY1-02E, passing over Ulansuhai Nur on 10 July and 13 July 2022, are shown in Figures 12 and 13. Water at Ulansuhai Nur was selected as a source for low-temperature calibration, while bare earth was used as a high-temperature calibration source. The mean DN of water area and bare soil area were extracted from satellite images, denoted as DN_{water} and DN_{soil}, respectively. Corresponding ground survey data were then calculated using radiative transfer, for conversion into radial brightness measurements used to calibrate the absolute radiation and the pupil for radiation calibration, as it shown in Table 2. The results of curve fitting are shown in Figure 9, while corresponding radiation calibration results are provided in Table 3. Figure 14 shows the calibration results for the of ZY1-02E IRS.

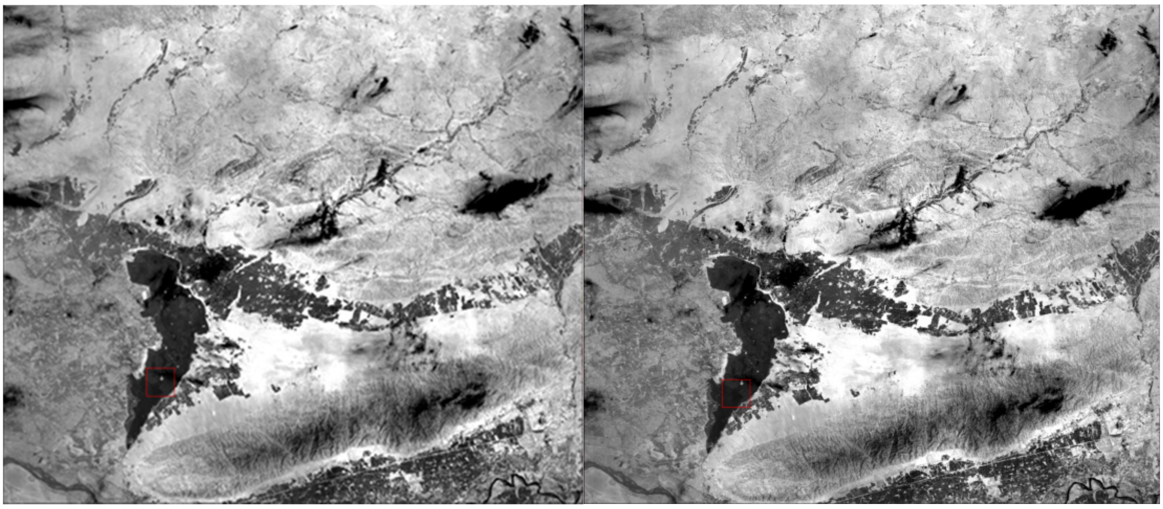

(**a**) (**b**)

Figure 12. Thermal infrared image data for Ulansuhai Nur (10 July 2022), including (**a**) sensor1 and (**b**) sensor2.

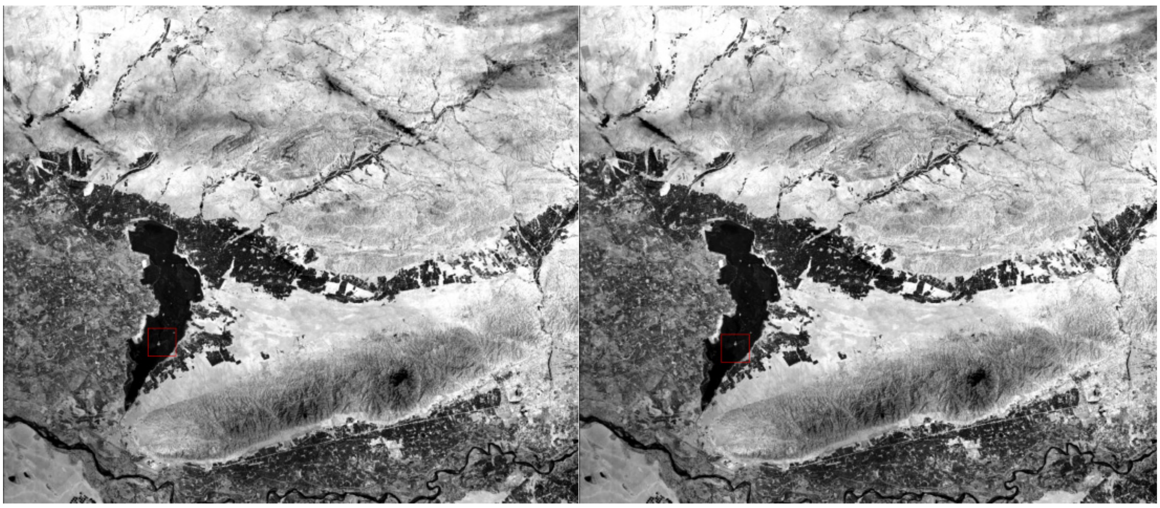

(**a**) sensor1 (**b**) sensor2

Figure 13. Thermal infrared image data for the Ulansuhai Nur experimental area (13 July 2022), including fitting results for (**a**) 20220710 and (**b**) 20220713 calibration coefficients.

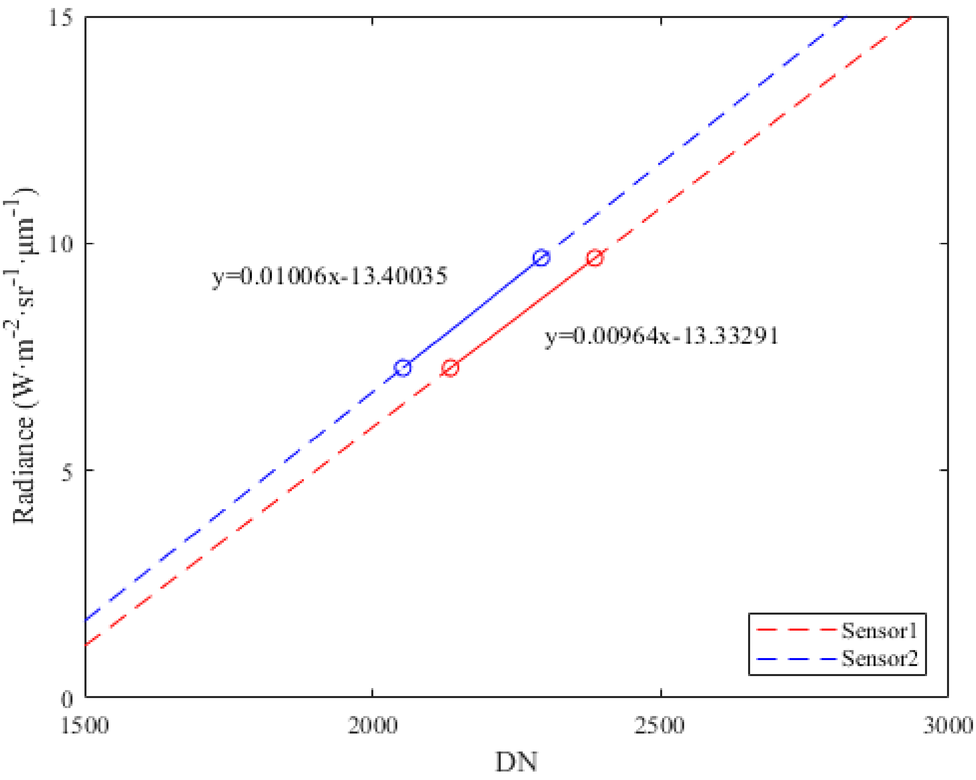

(**a**)

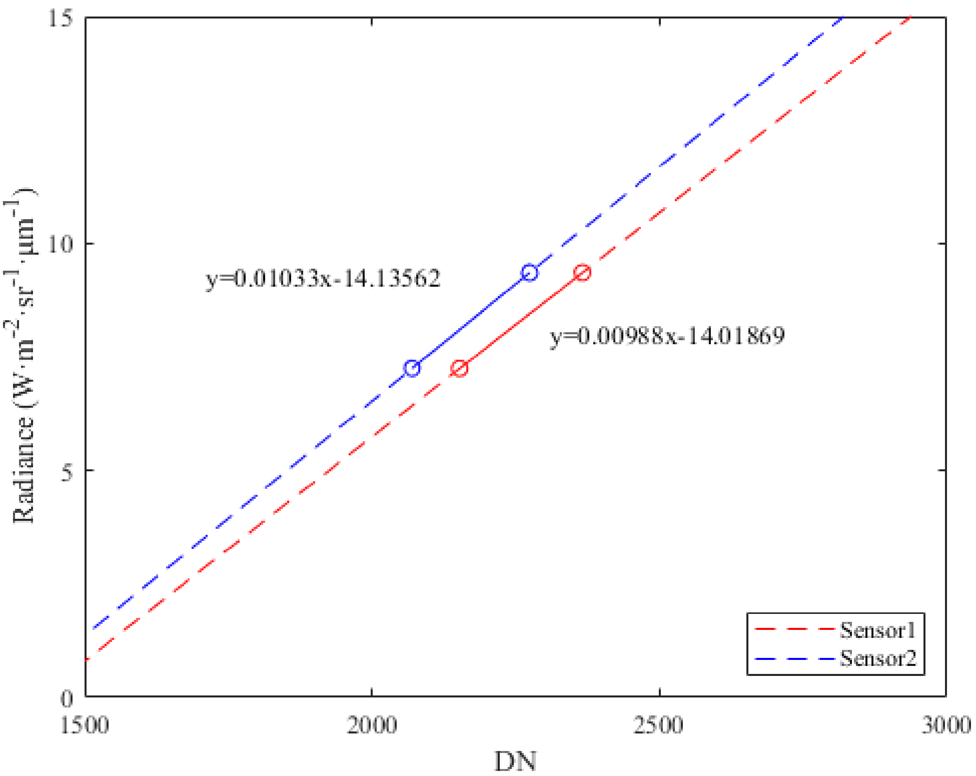

(**b**)

Figure 14. Fitting results for the calibration of ZY1-02E IRS in orbit: (**a**) 20220710 calibration coefficients; (**b**) 20220713 calibration coefficients.

Table 2. ZY1-02E and thermal IR camera parameters.

Date	Features	Sensor	DN Value	At-Sensor Radiance ($W \cdot m^{-2}\ sr^{-1}\ \mu m^{-1}$)
10 July 2022	Water	Sensor1	2134.7	7.2553
		Sensor2	2052.3	
	Bare Soil	Sensor1	2385.2	9.6713
		Sensor2	2292.3	
13 July 2022	Water	Sensor1	2152.4	7.2458
		Sensor2	2069.7	
	Bare Soil	Sensor1	2366.1	9.3569
		Sensor2	2274.1	

Table 3. IRS radiometric calibration results.

Date	Sensor	Calibration Coefficients ($W \cdot m^{-2}\ sr^{-1}\ \mu m^{-1}$)	
		Gain	Bias
10 July 2022	Sensor1	0.009644	13.3329
	Sensor2	0.010064	13.4003
13 July 2022	Sensor1	0.009879	14.0186
	Sensor2	0.010331	14.1356

4. Discussion

Uniform sandy land and vegetation in the Kubuqi Desert and Baotou field were selected as verification points. The mean regional DN was extracted from satellite thermal infrared images and a calibration coefficient was used to calculate the on-satellite entry pupil radiance, determined by radiative transmission using ground measurement data for comparison and verification. Table 4 shows a series of verification results using field synchronous measurement data in radiative transfer simulations, projected from the satellite, to determine pupil equivalent radial brightness and light temperature. These radiation measurements are based on tests using on-orbit calibration coefficients, calculated using equivalent radial brightness and comparative analysis. Equivalent bright temperature deviations were less than 0.7 K for IRS Sensor1, with an RMSE of 0.5 K, and less than 0.8 K for Sensor2, with an RMSE of 0.52 K. These results demonstrate the proposed calibration method offers high accuracy.

The sources of uncertainties in ZY1-02E thermal infrared camera primarily included the following:

(1) Measurement uncertainties for off-water radiance—The 102F Fourier transform thermal infrared spectrometer used in this experiment synchronously measured water during satellite transit, measuring off-water radiance with an accuracy higher than 0.1 K.

(2) Measurement uncertainties in the infrared temperature sensor—The SI-111 infrared temperature sensor was used to measure off-ground brightness temperatures for ground targets during satellite transit. A temperature–radiance lookup table was established using Planck's law for conversion into off-ground radiance. The errors introduced in this process were ~0.2 K.

(3) Measurement uncertainties for atmospheric parameters—Water vapor content in the atmosphere is one of the most important factors affecting the calculation of radiative transmission in the thermal infrared band. During on-orbit calibration of Landsat 5 TM at Lake Tahoe, Hook et al. [17] observed a brightness temperature deviation of ~0.13 K

when the total water vapor content increased by 10%. In this paper, atmospheric parameters for the test area were obtained using a sounding balloon during satellite transit. Atmospheric aerosol and water vapor contents were measured by CE318, which greatly improved measurement accuracy for atmospheric parameters.

(4) Errors caused by simulated atmospheric radiative transmission—MODTRAN 6.0 was used in this experiment to simulate radiative transmission. Inherent model errors were less than 2%, which meets on-orbit radiative calibration requirements. The combined error, resulting from atmospheric parameter measurements and the radiative transfer model, was ~0.2–0.3 K.

In summary, calibration errors for the spaceborne thermal infrared cameras used in this experiment were ~0.5–0.6 K, as it shown in Table 4. The results of radiometric accuracy verification tests (using multiple homogeneous ground objects) also showed the on-orbit absolute radiometric calibration technique proposed in this paper achieved accuracy better than 0.6 K for thermal infrared cameras.

Table 4. On-orbit validation results for the calibration accuracy of ZY1-02E.

Date	Sensor	Feature	DN Value	Calculation Based on On-Orbit Calibration Coefficients		Model Simulation Based on Measured Data		Relative Radiance Deviation (%)	Equivalent Brightness Temperature Deviation ΔT (K)
				On-Satellite Radiance (W·m^{-2} sr^{-1} μm^{-1})	Equivalent Brightness Temperature (K)	At-Sensor Radiance (W·m^{-2} sr^{-1} μm^{-1})	Equivalent Brightness Temperature (K)		
10 July 2022	Sensor1	Baotou Sand	2354.1	9.3715	298.935	9.3045	298.354	0.720%	0.581
		Baotou Vegetation	2169.6	7.5921	287.778	7.5555	287.531	0.490%	0.247
		Kubuqi Desert	2270.3	8.5634	294.056	8.6478	294.58	−0.971%	0.523
	Sensor2	Baotou Sand	2260.9	9.3548	298.837	9.3045	298.354	0.537%	0.483
		Baotou Vegetation	2087.9	7.6142	287.926	7.5555	287.531	0.781%	0.395
		Kubuqi Desert	2181.8	8.559	294.029	8.6478	294.58	−1.029%	0.550
13 July 2022	Sensor1	Baotou Sand	2401.3	9.705	300.869	9.616	300.449	0.927%	0.420
		Baotou Vegetation	2167.2	7.3925	286.423	7.463	287.085	−0.950%	0.662
		Kubuqi Desert	2329.8	8.9988	296.72	9.112	297.291	−1.237%	0.571
	Sensor2	Baotou Sand	2310.7	9.7353	301.043	9.616	300.449	1.242%	0.594
		Baotou Vegetation	2083	7.3832	286.359	7.463	287.085	−1.075%	0.726
		Kubuqi Desert	2241.3	9.0181	296.836	9.112	297.291	−1.025%	0.455

Table 5 shows the sources of uncertainty in TOA radiance of ZY1-02E vicarious radiometric calibration. In summary, calibration uncertainty for the ZY1-02E thermal infrared cameras used in this experiment was ~0.5–0.6 K. The results of radiometric accuracy verification tests also showed the on-orbit absolute radiometric calibration technique proposed in this paper achieved accuracy better than 0.6 K for thermal infrared cameras.

Table 5. Sources of uncertainty in TOA radiance of ZY1-02E vicarious radiometric calibration.

Source of Uncertainty	Accuracy	TOA Radiance Uncertainty
Off-Water Radiance		0.1 K
SI-III Infrared Temperature Sensor		~0.2 K
Atmospheric Parameters	10%	~0.13 K
MODTRAN 6.0 Radiative Transfer	2%	~0.2–0.3 K
Overall Uncertainty		~0.5–0.6 K

5. Conclusions

Data from satellite–ground-synchronous observation tests conducted at Ulansuhai Nur and Baotou fields (Inner Mongolia, July 2022), involving a ZY1-02E thermal infrared camera, were used to develop an on-orbit absolute radiation calibration and verification technique based on a variety of natural features. Water and bare soil were selected as high- and low-temperature calibration sources to conduct on-orbit absolute radiometric calibration of a thermal infrared camera and to acquire corresponding calibration coefficients. A variety of natural features, including sandy terrain and vegetation were used as accuracy verification points to evaluate radiometric calibration results and coefficients. Results showed this method achieved accuracy better than 0.6 K for the ZY1-02E thermal infrared camera, providing support for the subsequent development of commercial thermal infrared data products at all levels and the rapid formation of application service capabilities.

Author Contributions: H.T. developed the research plan and supervised the work; J.X., X.D., H.Z., and W.C. participated in the literature review, method selection, data acquisition, and discussions. All authors have read and agreed to the published version of the manuscript.

Funding: This work was supported by the National Key R&D Program of China, 2022YFB3903000, 2022YFB3903005, 2022YFB3903200, 2022YFB3903201.

Data Availability Statement: Not applicable.

Conflicts of Interest: The authors declare no conflict of interest.

References

1. Van Der Meer, F.; Hecker, C.; Van Ruitenbeek, F.; Van der Werff, H.; De Wijkerslooth, C.; Wechsler, C. Geologic remote sensing for geothermal exploration: A review. *Int. J. Appl. Earth Obs. Geoinf.* **2014**, *33*, 255–269. [CrossRef]
2. Jimenez-Munoz, J.C.; Cristobal, J.; Sobrino, J.A.; Soria, G.; Ninyerola, M.; Pons, X.; Pons, X. Revision of the single-channel algorithm for land surface temperature retrieval from landsat thermal-infrared data. *IEEE Trans. Geosci. Remote Sens.* **2009**, *47*, 339–349. [CrossRef]
3. Zhao, S.; Wang, Q.; You, D.; Yao, Y.; Zhu, L.; Sui, X. Preliminary analysis on the application of satellite infrared remote sensing techniques in environmental protection of China. *J. Geo-Inf. Sci.* **2015**, *7*, 12–17.
4. Vaughan, W.W.; Johnson, D.L. Meteorological satellites—The very early years, prior to launch of tiros-1. *Bull. Am. Meteorol. Soc.* **1994**, *75*, 2295–2302. [CrossRef]
5. Ninomiya, Y.; Fu, B.H. Thermal infrared multispectral remote sensing of lithology and mineralogy based on spectral properties of materials. *Ore Geol. Rev.* **2019**, *108*, 54–72. [CrossRef]
6. Han, Q.J.; Liu, L.; Fu, Q.Y.; Zhang, X.W.; Wang, A.C.; Pan, Z.Q. Vicarious calibration of multiple sensors based on reanalysis data of pseudo-invariant site. *Acta Opt. Sin.* **2014**, *34*, 1128002.
7. Ohring, G.; Wielicki, B.; Spencer, R.; Emery, B.; Datla, R. Satellite instrument calibration for measuring global climate change: Report of a workshop. *Bull. Am. Meteorol. Soc.* **2005**, *86*, 1303–1314. [CrossRef]
8. Datla, R.U.; Rice, J.P.; Lykke, K.R.; Johnson, B.C.; Butler, J.J.; Xiong, X. Best practice guidelines for pre-launch characterization and calibration of instruments for passive optical remote sensing. *J. Res. Natl. Inst. Stand. Technol.* **2011**, *116*, 621–646. [CrossRef] [PubMed]
9. Zhang, Y.X.; Li, X.; Zhang, M.; Kang, Q.; Wei, W.; Zheng, X.B.; Zhang, Y. On-orbit radiometric calibration for thermal infrared band of fy3d/mersi-ii satellite remote sensor based on qinghai lake radiation calibration test-site. *Acta Photon. Sin.* **2020**, *49*, 128–136.
10. Barsi, J.A.; Schott, J.R.; Hook, S.J.; Raqueno, N.G.; Markham, B.L.; Radocinski, R.G. Landsat-8 thermal infrared sensor (tirs) vicarious radiometric calibration. *Remote Sens.* **2014**, *6*, 11607–11626. [CrossRef]
11. Okuyama, A.; Hashimoto, T.; Nakayama, R.; Tahara, Y.; Kurino, T.; Takenaka, H.; Fukuda, S.; Nakajima, T.Y.; Higurashi, A.; Sekiguchi, M. Geostationary imager visible channel recalibration. In Proceedings of the 2009 EUMETSAT Meteorological Satellite Conference, Bath, UK, 21–25 September 2009.
12. Schott, J.R.; Hook, S.J.; Barsi, J.A.; Markham, B.L.; Miller, J.; Padula, F.P.; Raqueno, N.G. Thermal infrared radiometric calibration of the entire landsat 4, 5, and 7 archive (1982–2010). *Remote Sens. Environ.* **2012**, *122*, 41–49. [CrossRef]
13. Zhang, Y.; Gu, H.F.; Yu, T.; Zhang, Y.X.; Chen, L.F.; Li, X.Y.; Li, X.W.; He, L.M. Absolute radiometric calibration of cbers-02 irmss thermal band. *Sci. China Ser. E* **2005**, *35*, 70–88. [CrossRef]
14. Rong, Z.G.; Qiu, K.M.; Hu, X.Q.; Zhang, Y.X. Comparison of pre-launch calibration in lab with the radiometric calibration in orbit for the fy-2 b meteorological satellite's ir channel. *J. Infrared Millim. Waves* **2002**, *21*, 408–412.
15. Han, Q.J.; Min, X.J.; Fu, Q.Y. In-flight absolute radiometric calibration for thermal infrared band of hj-1b. *J. Remote Sens.* **2010**, *14*, 1212–1225.

16. Liu, L.; Gu, X.F.; Yu, T.; Li, X.Y.; Gao, H.L.; Li, J.G.; Shi, T.T. Hj-1b thermal infrared band in-flight radiometric calibration and validation. *Infrared Laser Eng.* **2012**, *41*, 1119–1125.
17. Hook, S.J.; Chander, G.; Barsi, J.A.; Alley, R.E.; Abtahi, A.; Palluconi, F.D.; Markham, B.L.; Richards, R.C.; Schladow, S.G.; Helder, D.L. In-flight validation and recovery of water surface temperature with landsat-5 thermal infrared data using an automated high-altitude lake validation site at lake tahoe. *IEEE Trans. Geosci. Remote Sens.* **2004**, *42*, 2767–2776. [CrossRef]